

All-microwave manipulation of superconducting qubits with a fixed-frequency transmon coupler

Shotaro Shirai,^{1,*} Yuta Okubo,¹ Kohei Matsuura,²
 Alto Osada,^{1,3} Yasunobu Nakamura,^{2,4} and Atsushi Noguchi^{1,4,5,†}

¹*Komaba Institute for Science (KIS), The University of Tokyo, Meguro-ku, Tokyo, 153-8902, Japan*

²*Department of Applied Physics, Graduate School of Engineering,
 The University of Tokyo, Bunkyo-ku, Tokyo 113-8656, Japan*

³*PRESTO, Japan Science and Technology Agency, Kawaguchi-shi, Saitama*

⁴*RIKEN Center for Quantum Computing (RQC), Wako, Saitama 351-0198, Japan*

⁵*Inamori Research Institute for Science (InaRIS), Kyoto-shi, Kyoto 600-8411, Japan*

(Dated: August 8, 2023)

All-microwave control of fixed-frequency superconducting quantum computing circuits is advantageous for minimizing the noise channels and wiring costs. Here we introduce a swap interaction between two data transmons assisted by the third-order nonlinearity of a coupler transmon under a microwave drive. We model the interaction analytically and numerically and use it to implement an all-microwave controlled-Z gate. The gate based on the coupler-assisted swap transition maintains high drive efficiency and small residual interaction over a wide range of detuning between the data transmons.

Quantum information science has evolved with the discovery and proposal of promising applications and is now entering the phase of testing them using actual quantum hardware. However, currently-available quantum hardware is still vulnerable to environmental noise and energy loss. Hence, implementing quantum error correction [1, 2] in a scalable approach is essential to demonstrate their potential and is thus being pursued in many physical systems [3–8].

Superconducting circuits are one of the leading platforms toward realization of fault-tolerant quantum computing [9, 10]. Among various types of qubits, fixed-frequency transmon [11] is a promising building block thanks to its long coherence time and small wiring overhead. For the architecture using fixed-frequency transmons, various all-microwave two-qubit gates have been proposed [12–19], and the cross-resonance (CR) gate is the most commonly-used entangling gate [12, 20–22]. In those schemes, however, weak anharmonicity of transmons results in a residual static ZZ interaction, which causes coherent errors and reduces the fidelity of operations. Therefore, it is of importance to suppress the residual interaction while maintaining the gate operation speed. A widely-adopted method for the purpose is to set the detuning between neighboring transmons to be in the so-called straddling regime, i.e., within the limited anharmonicity [11], though there remain some unwanted higher-order transitions to be avoided. The so-called frequency-crowding problem hinders the straightforward design of the circuits [23, 24]. Recently, this problem has been addressed partially via frequency tuning using post-fabrication techniques such as laser annealing [25–28], but further tolerance in design parameters is still desirable.

In this study, we propose and experimentally demonstrate a drive-efficient single-excitation exchange inter-

action between two transmons that allows all-microwave controlled-Z (CZ) gate over a wide range of detuning between data transmons. In this scheme, the interaction is activated by applying a microwave drive to a coupler transmon whose third-order nonlinearity plays a central role. The process can be understood as four-wave mixing involving three qubits and a drive microwave photon. We have therefore named it Coupler-Assisted Swap (CAS) interaction or transition. Note that a similar mechanism is used to exchange a single photon between two cavities [29].

Remarkably, the CAS transition relies neither on the less-coherent higher energy levels outside the qubit subspace nor on the direct transverse coupling between the data transmons. At the same time, the latter can in turn be utilized for the suppression of unwanted ZZ coupling [22, 30]. This also widens the choice of the qubit detuning in the device design.

The circuit under consideration [Figs. 1(a) and (b)] consists of three fixed-frequency transmons, with the total Hamiltonian being modeled as coupled Duffing oscillators under the rotating-wave approximation,

$$\hat{H}/\hbar = \sum_i \left(\omega_i \hat{a}_i^\dagger \hat{a}_i + \frac{\alpha_i}{2} \hat{a}_i^\dagger \hat{a}_i^\dagger \hat{a}_i \hat{a}_i \right) + \sum_{i \neq c} g_{ic} (\hat{a}_i^\dagger \hat{a}_c + \hat{a}_i \hat{a}_c^\dagger), \quad (1)$$

where \hbar is the reduced Planck constant, ω_i and α_i ($i \in \{1, 2, c\}$) are the fundamental frequency and anharmonicity of each transmon, \hat{a}_i and \hat{a}_i^\dagger are the annihilation and creation operators, and g_{ic} is the transverse coupling strength between the data transmon Q_i and the coupler transmon Q_c . Here we assume the dispersive regime $|g_{ic}/\Delta_{ic}| \ll 1$, where $\Delta_{ic} = \omega_i - \omega_c$. For the moment, we omit the direct coupling between the data qubits, g_{12} , and consider up to the third excited state of each transmon.

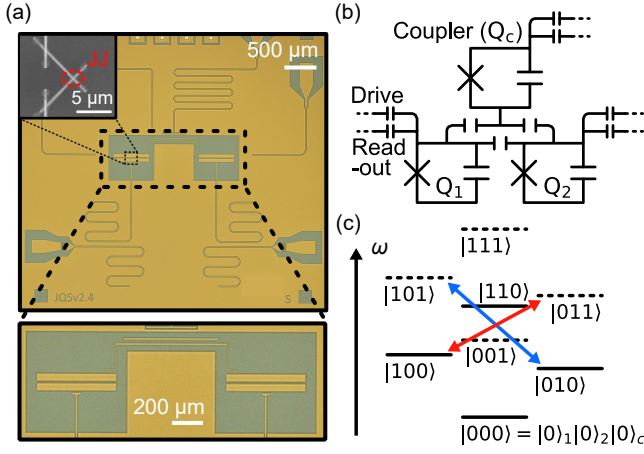


FIG. 1. (a) Optical images of a fabricated superconducting circuit (top) and three coupled transmons (bottom). Most of the structures are made from TiN electrodes (yellow) on a Si substrate (gray). Inset: Scanning electron micrograph of an Al/AIO_x/Al Josephson junction fabricated with the in-situ bandage technique [31]. (b) Equivalent circuit diagram of the coupled transmon system, where readout resonators, Purcell filters, and drive lines are omitted. Only the coupling capacitors connected to them are depicted. Q₁, Q₂, and Q_c represent the two data qubits and one coupler qubit, respectively. (c) Energy-level diagram of the system eigenstates $|ijk\rangle = |i\rangle_1 |j\rangle_2 |k\rangle_c$ ($i, j, k \in \{0, 1\}$) truncated to the first excited state of each transmon. The blue and red arrows are the CAS transitions activated by microwave drives. The dashed energy levels involve the single excitation of the coupler.

To induce the interaction between the data qubits, we apply a microwave drive

$$\hat{H}_d/\hbar = \Omega_d \cos \omega_d t (\hat{a}_c^\dagger + \hat{a}_c) \quad (2)$$

to the coupler qubit, where ω_d and Ω_d are the drive frequency and amplitude, respectively. To find an analytical expression of the induced CAS interaction strength, we expand the drive term to the second order of g_{ic} using the Schrieffer-Wolff transformation [See Supplemental Material]. Then, we obtain the effective drive term in the Hamiltonian,

$$\hat{H}'_d \approx \hat{H}_d + [\hat{S}, \hat{H}_d] + \frac{1}{2} [\hat{S}_1, [\hat{S}_1, \hat{H}_d]], \quad (3)$$

where the anti-Hermitian operator $\hat{S} = \hat{S}_1 + \hat{S}_2$ fulfills the conditions

$$[\hat{H}_0, \hat{S}_1] + \hat{O}_1 = 0, \quad (4)$$

$$[\hat{H}_0, \hat{S}_2] + \hat{O}_2 = 0. \quad (5)$$

Here, \hat{O}_1 is the off-diagonal part of Eq. (1), corresponding to the coupling term, and \hat{H}_0 is the rest. \hat{O}_2 is the off-diagonal part of $\frac{1}{2} [\hat{O}_1, \hat{S}_1]$. The effective drive term, Eq. (3), due to the third-order nonlinearity of the coupler, contains many transition matrix elements between

eigenstates in the Hilbert space spanned by the three transmons. Among them, we focus on the CAS transitions between data qubits assisted by the single-photon excitation of the nonlinear coupler, such as $|010\rangle \leftrightarrow |101\rangle$ and $|100\rangle \leftrightarrow |011\rangle$, respectively illustrated by the blue and red arrows in Fig. 1(c), where $|ijk\rangle = |i\rangle_1 |j\rangle_2 |k\rangle_c$ ($i, j, k \in \{0, 1\}$). Here, we refer to them as the blue and red CAS transitions at the frequencies of ω_b and ω_r , respectively. We also assume $\omega_1 > \omega_2$ without loss of generality. From Eq. (3), analytical expressions for the drive-induced oscillation frequencies are calculated under the rotating-wave approximation as

$$\begin{aligned} \Omega_b &\approx 2 \langle 010 | \hat{H}'_d | 101 \rangle / \hbar \\ &= \frac{2g_{1c}g_{2c}\alpha_c\Omega_d}{\Delta_{12}(\omega_c - \omega_1 + \alpha_c)(\omega_c - \omega_2)}, \end{aligned} \quad (6)$$

$$\begin{aligned} \Omega_r &\approx 2 \langle 100 | \hat{H}'_d | 011 \rangle / \hbar \\ &= \frac{-2g_{1c}g_{2c}\alpha_c\Omega_d}{\Delta_{12}(\omega_c - \omega_2 + \alpha_c)(\omega_c - \omega_1)}, \end{aligned} \quad (7)$$

respectively for the blue and red CAS transitions, where $\Delta_{12} = \omega_1 - \omega_2$. The CAS-based CZ gate can be realized by applying a resonant 2π -pulse of the blue (red) CAS transition, where the state $|010\rangle$ ($|100\rangle$) acquires the geometric phase of π after a round trip [32].

In the experiment, we use a circuit consisting of three capacitively coupled fixed-frequency transmons [11], two $\lambda/4$ coplanar-waveguide (CPW) readout resonators and Purcell filters [35] for data transmons, and one $\lambda/2$ -CPW readout resonator for the coupler transmon [Fig. 1(a)]. The device parameters are the following: The fundamental frequencies of the data transmons and the coupler transmon are $\omega_1/2\pi \simeq 5.641$ GHz, $\omega_2/2\pi \simeq 5.507$ GHz and $\omega_c/2\pi \simeq 6.317$ GHz, respectively. The third-order nonlinearities of the transmons are $\alpha_1/2\pi \simeq -300$ MHz, $\alpha_2/2\pi \simeq -303$ MHz and $\alpha_c/2\pi \simeq -381$ MHz, and the transverse coupling strengths between the data transmons and the coupler transmon are $g_{1c}/2\pi \simeq 40$ MHz and $g_{2c}/2\pi \simeq 31$ MHz. The direct transverse coupling between data transmons is estimated to be $g_{12}/2\pi \simeq 1.9$ MHz by fitting the measurement result of the ZZ interaction, and the static ZZ interaction strength between data transmons is estimated as $\xi_0/2\pi \simeq -1.5$ kHz [See Supplemental Material]. The transmons, Q₁, Q₂ and Q_c, have energy relaxation times T_1 of 95 μ s, 108 μ s and 15 μ s, Ramsey dephasing times T_2^* of 76 μ s, 81 μ s and 15 μ s, and echo dephasing times T_2^e of 88 μ s, 166 μ s and 18 μ s, respectively. Part of the reason for the lower coherence of the coupler transmon is presumably due to its narrower electrodes and concentrated electric field [36]. This can be improved by design modifications.

For single-qubit gates, we use a Gaussian pulse with its FWHM $\sigma = 7.5$ ns, total gate length 4σ , and with derivative removal by adiabatic modulation (DRAG) [37]. For the CAS transitions, we apply to the coupler a flat-top drive pulse with Gaussian-shaped edges of $\sigma = 10$ ns and

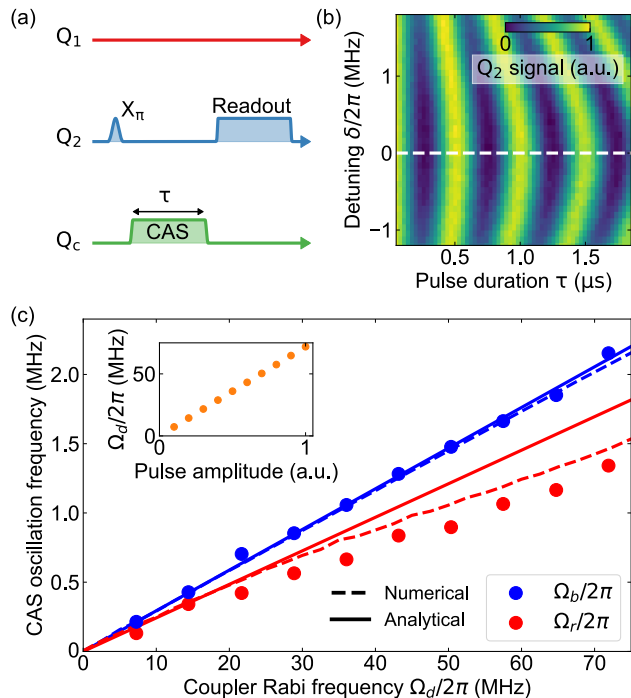


FIG. 2. (a) Pulse sequence for the data transmons, Q_1 and Q_2 , and the coupler transmon Q_c to measure the CAS oscillation frequency between the states indicated by the blue arrow in Fig. 1(c). To activate the transition, we prepare Q_2 in the first excited state with a π pulse, and then apply a drive pulse to the coupler. (b) Chevron pattern of the blue CAS transition as a function of the detuning $\delta = \omega_d - \omega_b$ and the pulse duration τ . The white dashed line, $\delta = 0$, shows the resonance condition for the blue CAS transition at $\omega_b/2\pi \simeq 6.4207$ GHz. The data is obtained for the coupler drive amplitude $\Omega_d/2\pi = 72$ MHz. Note that the blue CAS transition frequency ω_b depends on Ω_d through the ac Stark shift and the associated correlated oscillations of the excited-state populations of the three transmons are separately observed [See Supplemental Material]. (c) Blue and red CAS oscillation frequencies obtained from the fitting. The blue and red solid lines are analytical evaluations respectively using Eqs. (6) and (7) with experimentally-determined parameters. The dashed lines are the numerical simulations based on Eqs. (1) and (2) using QuTiP [33, 34]. Inset: Ω_d calibration result by driving the fundamental mode of the coupler qubit as a function of the pulse amplitude.

a total edge length of 4σ .

We first measure the CAS oscillation frequencies as a function of the drive amplitude Ω_d . As shown in Fig. 2(a), for the blue CAS transition, we prepare the system in $|010\rangle$ and then apply a coupler drive with a given Ω_d and with various drive frequencies and pulse lengths. By fitting the resulting oscillations in the excited state population of Q_2 [Fig. 2(b)], we obtain the oscillation frequency Ω_b , which is plotted with blue dots in Fig. 2(c) as a function of Ω_d . Similarly, Ω_r for the red CAS transition is obtained.

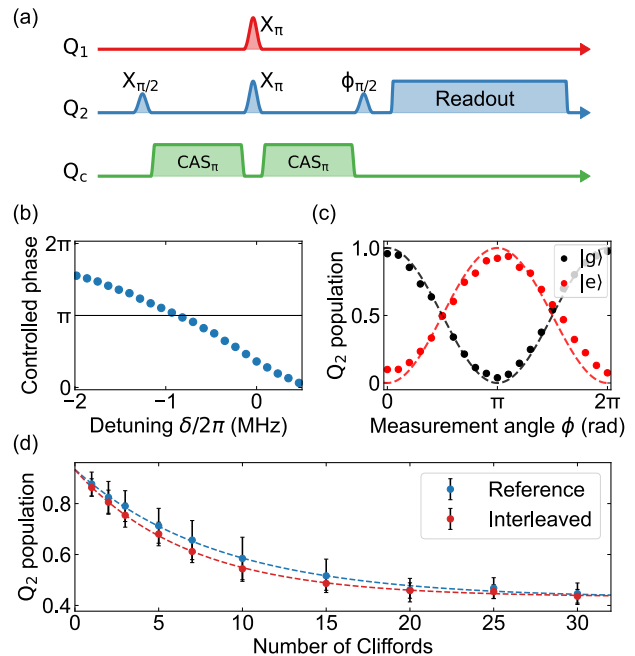


FIG. 3. (a) Pulse sequence for measuring the control phase using the Joint Amplification of ZZ (JAZZ) protocol [38, 39]. The measurement angle ϕ is swept to find an optimal CAS drive frequency for the CZ gate. (b) Controlled phase measured as a function of $\delta = \omega_d - \omega_b$, where $\omega_b/2\pi \simeq 6.4157$ GHz for the drive amplitude of $\Omega_d/2\pi = 75$ MHz. For each drive frequency, we adjust the pulse length so that the coupler returns to the ground state. (c) Ramsey fringes measured with the calibrated detuning of the blue CAS drive. A π phase shift is observed depending on the states of the control transmon Q_1 . The vertical axis is the signal of Q_2 normalized to the responses of the ground and excited states of Q_2 . The black and red dashed curves represent the functions of the ideal CZ gate. (d) Interleaved randomized benchmarking (IRB). Blue and red dots are the averaged experimental results of the reference RB and IRB, respectively. The number of randomly-generated RB sequences used is 30, and the error bars represent 95% confidence. Dashed lines are fitting curves to the decay model. The horizontal axis is the number of Clifford gates applied. All single-qubit Clifford gates consist of two $X_{\pi/2}$ gates and three virtual-Z gates, and the length of the CZ gate is 504 ns. Thus, the average duration of the two-qubit Clifford gate is 945 ns, where each spacing between two successive pulses is set to 6 ns [40].

To check the validity of our theoretical model, we also plot in Fig. 2(c) the analytically obtained values from Eqs. (6) and (7) and the numerical ones from Eqs. (1) and (2). For the blue CAS transition, our model is in good agreement with the experimental result. For the red CAS transition, the numerical calculation is also in good agreement with the experimental result, but the analytical model shows a deviation in the strong drive regime. This could be an off-resonant effect of a single-photon transition ($|110\rangle \leftrightarrow |201\rangle$) and two-photon transitions ($|000\rangle \leftrightarrow |002\rangle$, $|010\rangle \leftrightarrow |102\rangle$) near ω_r . The

blue CAS oscillation frequency fits better as there are no near disturbing transitions on the higher frequency side of ω_c because of the negative anharmonicity of the transmon. This can be an advantage for relaxing the frequency crowding problem.

We next implement the CZ gate using the blue CAS transition. We first determine the relation between the CAS drive detuning and the pulse duration by fitting the chevron pattern with the drive amplitude $\Omega_d/2\pi = 75$ MHz, which is slightly larger than the experiments presented in Fig. 2 and the resulting blue CAS oscillation frequency is about 2.2 MHz. We then calibrate the amount of controlled phase shift using the Joint Amplification of ZZ (JAZZ) sequence [38, 39] shown in Fig. 3(a). In this sequence, Q_2 is detected in the excited state when the amount of the controlled phase shift is π and the final measurement angle ϕ is 0. By sweeping ϕ and fitting the result with a cosine function, the amount of the control phase is obtained from the phase shift of the cosine function. Figure 3(b) shows the obtained phase shift as a function of the CAS drive detuning. The optimal drive frequency and flat-top duration are obtained by interpolating the result. The associated local phase shift induced by the CAS drive on each qubit is evaluated and canceled with a virtual-Z gate [41] to implement the CAS-based CZ gate. Through the interleaved randomized benchmarking (IRB) [42] of the calibrated CAS-based CZ gate, a fidelity of 97.8(6)% is obtained [Fig. 3(d)]. The master-equation simulation with our device parameters yields 97.8% fidelity for the CZ gate, which is mainly limited by the short coherence time of the coupler qubit. This implies that the CAS-based CZ gate can be improved further by optimizing the design parameter and coherence time of the coupler.

Finally, using Figs. 4(a) and (b), we discuss dependencies of the residual ZZ interaction strength between the data qubits, ξ_{ZZ} , and the drive efficiency of the blue CAS-based CZ gate rate, $\eta_b = \Omega_b/\Omega_d$, on the current and prospective design parameters. Here, we numerically diagonalize Eq. (1) to calculate the residual ZZ-interaction strength when the coupler is in the ground state. Note that in these calculations, the term $g_{12}(\hat{a}_1^\dagger\hat{a}_2 + \hat{a}_1\hat{a}_2^\dagger)$, which has been ignored so far, is added to Eq. (1) to see the effect of direct coupling. As reported in previous studies [22, 30], the direct coupling g_{12} can suppress the residual ZZ interaction by canceling the one mediated by the coupler. As shown in Fig. 4(a), the straddling regime ($|\Delta_{12}/\alpha_{\text{mean}}| < 1$) gives high drive efficiency and low residual ZZ interaction for the parameter set. On the other hand, we can also achieve practical performance far outside the straddling regime by selecting appropriate values of parameters, especially of g_{12} . In Fig. 4(b), we set $g_{12}/2\pi = 5$ MHz as an example. This parameter set enables implementation of the blue CAS-based CZ gates of 100–200 ns for $\Omega_d/2\pi = 200$ MHz in a wide range of the detuning ($2 \lesssim \Delta_{12}/\alpha_{\text{mean}} \lesssim 4$) between the

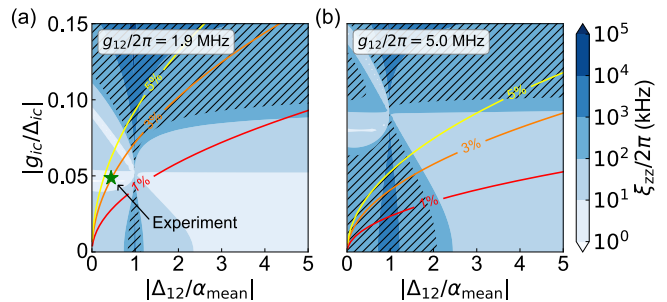


FIG. 4. Residual ZZ interaction strength ξ_{ZZ} and the drive efficiency η_b of the blue CAS transition as a function of the detuning Δ_{12} and transverse coupling strength g_{1c} normalized by the mean anharmonicity $\alpha_{\text{mean}} = (\alpha_1 + \alpha_2)/2$ and detuning Δ_{ic} , ($i \in \{1, 2\}$), respectively. Here, ξ_{ZZ} is calculated through numerical diagonalization of Eq. (1) (filled contour plot) using (a) the current and (b) prospective design parameters with the direct transverse coupling g_{12} . The drive efficiency is defined as $\eta_b = \Omega_b/\Omega_d$ from Eq. (6) (contour line plot). As the prospective design parameters, we set $(\omega_c - \omega_1)/2\pi = 0.6$ GHz, $\omega_2/2\pi = 5.0$ GHz, and $\alpha_i/2\pi = (-0.20, -0.20, -0.45)$ GHz for $i = (1, 2, c)$. The sweep parameters are ω_1 and $g_{1c}/\Delta_{1c} = g_{2c}/\Delta_{2c}$, and the shaded areas indicate the residual ZZ interaction strength larger than 150 kHz. The green star in (a) indicates the condition in the current experiment.

data transmons while keeping the residual ZZ coupling < 100 kHz. The coherent error due to the residual ZZ interaction during the non-commuting single-qubit gates can be mitigated with an optimal-control pulse [43, 44] or a composite pulse robust to frequency shift [45, 46]. We can also apply an active residual ZZ interaction cancellation using an off-resonant microwave drive near the blue CAS transition [See Supplemental Material] or coupler-qubit transition [47].

In conclusion, we have investigated and analytically modeled the four-wave-mixing interaction among three superconducting qubits under a microwave drive. By using the interaction, we demonstrated the coupler-assisted-swap-based control-Z gate between two fixed-frequency transmons mediated by a fixed-frequency transmon coupler. The drive efficiency of the gate has a practical value in a wide parameter range, providing an alternative solution to the frequency crowding problem and a new design paradigm for superconducting quantum processors. Moreover, a physically-efficient parity measurement could be realized by measuring the coupler after a pulse sequence of simultaneous π -pulses to the blue and red CAS transitions. An alternative pulse sequence of two π -pulses to the blue (red) CAS transition sandwiching π -pulses to the data qubits would also work.

Acknowledgement—The authors acknowledge K. Kusuyama, K. Nittoh, and L. Szikszai for their support in the device fabrication, H. Terai and Y. Hishida for providing the TiN films, H. Goto, M. Shigefuji, and K.

Taniguchi for fruitful discussions, and Y. Sunada, K. Heya, and T. Miyamura for sharing the measurement codes. This work was partly supported by JST ERATO (Grant No. JPMJER1601), MEXT Q-LEAP (Grant No. JPMXS0118068682), and JSPS KAKENHI (Grant No. JP22J15257).

Data availability—The experimental datasets and source codes used to generate the results of this manuscript are available in the [Zenodo], at [<https://doi.org/10.5281/zenodo.7885632>].

* shirai-shotaro@ecc.u-tokyo.ac.jp

† u-atsushi@ecc.u-tokyo.ac.jp

- [1] A. Kitaev, *Annals of Physics* **303**, 2 (2003).
- [2] S. B. Bravyi and A. Y. Kitaev, *arXiv preprint quant-ph/9811052* (1998).
- [3] T. D. Ladd, F. Jelezko, R. Laflamme, Y. Nakamura, C. Monroe, and J. L. O’Brien, *Nature* **464**, 45 (2010).
- [4] M. Kjaergaard, M. E. Schwartz, J. Braumüller, P. Krantz, J. I.-J. Wang, S. Gustavsson, and W. D. Oliver, *Annual Review of Condensed Matter Physics* **11**, 369 (2020).
- [5] K. R. Brown, J. Kim, and C. Monroe, *npj Quantum Information* **2**, 16034 (2016).
- [6] M. Saffman, *Journal of Physics B: Atomic, Molecular and Optical Physics* **49**, 202001 (2016).
- [7] C. Koeffel and D. Loss, *Annual Review of Condensed Matter Physics* **4**, 51 (2013).
- [8] S. Slussarenko and G. J. Pryde, *Applied Physics Reviews* **6**, 041303 (2019).
- [9] P. Krantz, M. Kjaergaard, F. Yan, T. P. Orlando, S. Gustavsson, and W. D. Oliver, *Applied Physics Reviews* **6**, 021318 (2019).
- [10] Z. Chen, K. J. Satzinger, J. Atalaya, A. N. Korotkov, A. Dunsforth, D. Sank, C. Quintana, M. McEwen, R. Barends, P. V. Klimov, S. Hong, C. Jones, A. Petukhov, D. Kafri, S. Demura, B. Burkett, C. Gidney, A. G. Fowler, A. Paler, H. Putterman, I. Aleiner, F. Arute, K. Arya, R. Babbush, J. C. Bardin, A. Bengtsson, A. Bourassa, M. Broughton, B. B. Buckley, D. A. Buell, N. Bushnell, B. Chiaro, R. Collins, W. Courtney, A. R. Derk, D. Eppens, C. Erickson, E. Farhi, B. Foxen, M. Giustina, A. Greene, J. A. Gross, M. P. Harrigan, S. D. Harrington, J. Hilton, A. Ho, T. Huang, W. J. Huggins, L. B. Ioffe, S. V. Isakov, E. Jeffrey, Z. Jiang, K. Kechedzhi, S. Kim, A. Kitaev, F. Kostritsa, D. Landhuis, P. Laptev, E. Lucero, O. Martin, J. R. McClean, T. McCourt, X. Mi, K. C. Miao, M. Mohseni, S. Montazeri, W. Mruczkiewicz, J. Mutus, O. Naaman, M. Neeley, C. Neill, M. Newman, M. Y. Niu, T. E. O’Brien, A. Opremcak, E. Ostby, B. Pató, N. Redd, P. Roushan, N. C. Rubin, V. Shvarts, D. Strain, M. Szalay, M. D. Trevithick, B. Villalonga, T. White, Z. J. Yao, P. Yeh, J. Yoo, A. Zalcman, H. Neven, S. Boixo, V. Smelyanskiy, Y. Chen, A. Megrant, J. Kelly, and G. Q. Ai, *Nature* **595**, 383 (2021).
- [11] J. Koch, T. M. Yu, J. Gambetta, A. A. Houck, D. I. Schuster, J. Majer, A. Blais, M. H. Devoret, S. M. Girvin, and R. J. Schoelkopf, *Phys. Rev. A* **76**, 042319 (2007).
- [12] C. Rigetti and M. Devoret, *Phys. Rev. B* **81**, 134507 (2010).
- [13] S. Poletto, J. M. Gambetta, S. T. Merkel, J. A. Smolin, J. M. Chow, A. D. Córcoles, G. A. Keefe, M. B. Rothwell, J. R. Rozen, D. W. Abraham, C. Rigetti, and M. Steffen, *Phys. Rev. Lett.* **109**, 240505 (2012).
- [14] J. M. Chow, J. M. Gambetta, A. W. Cross, S. T. Merkel, C. Rigetti, and M. Steffen, *New Journal of Physics* **15**, 115012 (2013).
- [15] H. Paik, A. Mezzacapo, M. Sandberg, D. T. McClure, B. Abdo, A. D. Córcoles, O. Dial, D. F. Bogorin, B. L. T. Plourde, M. Steffen, A. W. Cross, J. M. Gambetta, and J. M. Chow, *Phys. Rev. Lett.* **117**, 250502 (2016).
- [16] A. Noguchi, A. Osada, S. Masuda, S. Kono, K. Heya, S. P. Wolski, H. Takahashi, T. Sugiyama, D. Lachance-Quirion, and Y. Nakamura, *Phys. Rev. A* **102**, 062408 (2020).
- [17] S. Krinner, P. Kurpiers, B. Royer, P. Magnard, I. Tsitsilin, J.-C. Besse, A. Remm, A. Blais, and A. Wallraff, *Phys. Rev. Applied* **14**, 044039 (2020).
- [18] B. K. Mitchell, R. K. Naik, A. Morvan, A. Hashim, J. M. Kreikebaum, B. Marinelli, W. Lavrijsen, K. Nowrouzi, D. I. Santiago, and I. Siddiqi, *Phys. Rev. Lett.* **127**, 200502 (2021).
- [19] K. Heya and N. Kanazawa, *PRX Quantum* **2**, 040336 (2021).
- [20] J. M. Chow, A. D. Córcoles, J. M. Gambetta, C. Rigetti, B. R. Johnson, J. A. Smolin, J. R. Rozen, G. A. Keefe, M. B. Rothwell, M. B. Ketchen, and M. Steffen, *Phys. Rev. Lett.* **107**, 080502 (2011).
- [21] S. Sheldon, E. Magesan, J. M. Chow, and J. M. Gambetta, *Phys. Rev. A* **93**, 060302(R) (2016).
- [22] A. Kandala, K. X. Wei, S. Srinivasan, E. Magesan, S. Carnevale, G. A. Keefe, D. Klaus, O. Dial, and D. C. McKay, *Phys. Rev. Lett.* **127**, 130501 (2021).
- [23] M. Malekakhlagh, E. Magesan, and D. C. McKay, *Phys. Rev. A* **102**, 042605 (2020).
- [24] A. Morvan, L. Chen, J. M. Larson, D. I. Santiago, and I. Siddiqi, *Phys. Rev. Research* **4**, 023079 (2022).
- [25] C. Granata, A. Vettoliere, L. Petti, M. Rippa, B. Ruggiero, P. Mormile, and M. Russo, in *Journal of Physics: Conference Series*, Vol. 97 (IOP Publishing, 2008) p. 012110.
- [26] J. B. Hertzberg, E. J. Zhang, S. Rosenblatt, E. Magesan, J. A. Smolin, J.-B. Yau, V. P. Adiga, M. Sandberg, M. Brink, J. M. Chow, and J. S. Orcutt, *npj Quantum Information* **7**, 129 (2021).
- [27] E. J. Zhang, S. Srinivasan, N. Sundaresan, D. F. Bogorin, Y. Martin, J. B. Hertzberg, J. Timmerwilke, E. J. Pritchett, J.-B. Yau, C. Wang, W. Landers, E. P. Lewandowski, A. Narasgond, S. Rosenblatt, G. A. Keefe, I. Lauer, M. B. Rothwell, D. T. McClure, O. E. Dial, J. S. Orcutt, M. Brink, and J. M. Chow, *Science Advances* **8**, eabi6690 (2022).
- [28] H. Kim, C. Jünger, A. Morvan, E. S. Barnard, W. P. Livingston, M. V. P. Altoé, Y. Kim, C. Song, L. Chen, J. M. Kreikebaum, D. F. Ogletree, D. I. Santiago, and I. Siddiqi, *Applied Physics Letters* **121**, 142601 (2022).
- [29] R. Lescanne, S. Deléglise, E. Albertinale, U. Réglade, T. Capelle, E. Ivanov, T. Jacqmin, Z. Leghtas, and E. Flurin, *Phys. Rev. X* **10**, 021038 (2020).
- [30] P. Mundada, G. Zhang, T. Hazard, and A. Houck, *Phys. Rev. Applied* **12**, 054023 (2019).
- [31] A. Osman, J. Simon, A. Bengtsson, S. Kosen, P. Krantz,

- D. P. Lozano, M. Scigliuzzo, P. Delsing, J. Bylander, and A. Fadavi Roudsari, *Applied Physics Letters* **118**, 064002 (2021).
- [32] E. Sjöqvist, *International Journal of Quantum Chemistry* **115**, 1311 (2015).
- [33] J. Johansson, P. Nation, and F. Nori, *Computer Physics Communications* **183**, 1760 (2012).
- [34] J. Johansson, P. Nation, and F. Nori, *Computer Physics Communications* **184**, 1234 (2013).
- [35] M. D. Reed, B. R. Johnson, A. A. Houck, L. DiCarlo, J. M. Chow, D. I. Schuster, L. Frunzio, and R. J. Schoelkopf, *Applied Physics Letters* **96**, 203110 (2010).
- [36] C. E. Murray, J. M. Gambetta, D. T. McClure, and M. Steffen, *IEEE Transactions on Microwave Theory and Techniques* **66**, 3724 (2018).
- [37] F. Motzoi, J. M. Gambetta, P. Rebentrost, and F. K. Wilhelm, *Phys. Rev. Lett.* **103**, 110501 (2009).
- [38] J. Garbow, D. Weitekamp, and A. Pines, *Chemical Physics Letters* **93**, 504 (1982).
- [39] J. Ku, X. Xu, M. Brink, D. C. McKay, J. B. Hertzberg, M. H. Ansari, and B. L. T. Plourde, *Phys. Rev. Lett.* **125**, 200504 (2020).
- [40] R. Barends, J. Kelly, A. Megrant, A. Veitia, D. Sank, E. Jeffrey, T. C. White, J. Mutus, A. G. Fowler, B. Campbell, Y. Chen, Z. Chen, B. Chiaro, A. Dunsworth, C. Neill, P. O'Malley, P. Roushan, A. Vainsencher, J. Wenner, A. N. Korotkov, A. N. Cleland, and J. M. Martinis, *Nature* **508**, 500 (2014).
- [41] D. C. McKay, C. J. Wood, S. Sheldon, J. M. Chow, and J. M. Gambetta, *Phys. Rev. A* **96**, 022330 (2017).
- [42] E. Magesan, J. M. Gambetta, B. R. Johnson, C. A. Ryan, J. M. Chow, S. T. Merkel, M. P. da Silva, G. A. Keefe, M. B. Rothwell, T. A. Ohki, M. B. Ketchen, and M. Steffen, *Phys. Rev. Lett.* **109**, 080505 (2012).
- [43] N. Khaneja, T. Reiss, C. Kehlet, T. Schulte-Herbrüggen, and S. J. Glaser, *Journal of Magnetic Resonance* **172**, 296 (2005).
- [44] Y. Baum, M. Amico, S. Howell, M. Hush, M. Liuzzi, P. Mundada, T. Merkh, A. R. R. Carvalho, and M. J. Biercuk, *PRX Quantum* **2**, 040324 (2021).
- [45] H. K. Cummins, G. Llewellyn, and J. A. Jones, *Phys. Rev. A* **67**, 042308 (2003).
- [46] H. K. Cummins and J. A. Jones, *New Journal of Physics* **2**, 6 (2000).
- [47] Z. Ni, S. Li, L. Zhang, J. Chu, J. Niu, T. Yan, X. Deng, L. Hu, J. Li, Y. Zhong, S. Liu, F. Yan, Y. Xu, and D. Yu, *Phys. Rev. Lett.* **129**, 040502 (2022).
- [48] R. Winkler, *Spin-Orbit Coupling Effects in Two-Dimensional Electron and Hole Systems*, Tracts in Modern Physics (Springer, Berlin, 2003).
- [49] M. Leskes, P. Madhu, and S. Vega, *Progress in Nuclear Magnetic Resonance Spectroscopy* **57**, 345 (2010).
- [50] C. J. Wood and J. M. Gambetta, *Phys. Rev. A* **97**, 032306 (2018).
- [51] D. I. Schuster, A. Wallraff, A. Blais, L. Frunzio, R.-S. Huang, J. Majer, S. M. Girvin, and R. J. Schoelkopf, *Phys. Rev. Lett.* **94**, 123602 (2005).
- [52] A. Schneider, J. Braumüller, L. Guo, P. Stehle, H. Rotzinger, M. Marthaler, A. V. Ustinov, and M. Weides, *Phys. Rev. A* **97**, 062334 (2018).
- [53] S. Zeytinoğlu, M. Pechal, S. Berger, A. A. Abdumalikov, A. Wallraff, and S. Filipp, *Phys. Rev. A* **91**, 043846 (2015).
- [54] E. Magesan and J. M. Gambetta, *Phys. Rev. A* **101**, 052308 (2020).

Supplemental Material for “All-microwave manipulation of superconducting qubits with a fixed-frequency transmon coupler”

Shotaro Shirai,^{1,*} Yuta Okubo,¹ Kohei Matsuura,²
 Alto Osada,^{1,3} Yasunobu Nakamura,^{2,4} and Atsushi Noguchi^{1,4,5,†}

¹*Komaba Institute for Science (KIS), The University of Tokyo, Meguro-ku, Tokyo, 153-8902, Japan*

²*Department of Applied Physics, Graduate School of Engineering,
 The University of Tokyo, Bunkyo-ku, Tokyo 113-8656, Japan*

³*PRESTO, Japan Science and Technology Agency, Kawaguchi-shi, Saitama*

⁴*RIKEN Center for Quantum Computing (RQC), Wako, Saitama 351-0198, Japan*

⁵*Inamori Research Institute for Science (InaRIS), Kyoto-shi, Kyoto 600-8411, Japan*

(Dated: August 8, 2023)

Sample and the experimental setup

The transmon qubits and the resonators are fabricated on a high-resistivity Si substrate. They are made from a sputtered and lithographically-patterned TiN film and Al/AlO_x/Al Josephson junctions evaporated and lifted off with the in-situ bridge-free bandage technique. As shown in Fig. S1(a), each input line of the dilution refrigerator has about 56-dB attenuation at 8 GHz including the cable loss. Each input line also has an eccosorb filter, an 8-GHz lowpass filter, and an extra 6-dB (20-dB) attenuator for the qubit (resonator) drive line. The sample is mounted inside a three-layer magnetic shield and cooled down to ~10 mK. Microwave pulses are generated by the single sideband modulation (SSB) [Figs. S1(b) and (c)]. The reflection pulses of the readout resonators are amplified with a low-noise HEMT amplifier at the 4-K stage and demodulated to IQ signals for the data processing [Fig. S1(d)]. The readout resonator frequencies are $\omega_r^1/2\pi \simeq 7.436$ GHz, $\omega_r^2/2\pi \simeq 7.375$ GHz and $\omega_r^c/2\pi \simeq 7.551$ GHz, respectively. The dispersive shifts of the readout resonators are less than 1 MHz, and the qubit energy relaxation through the readout line is negligible.

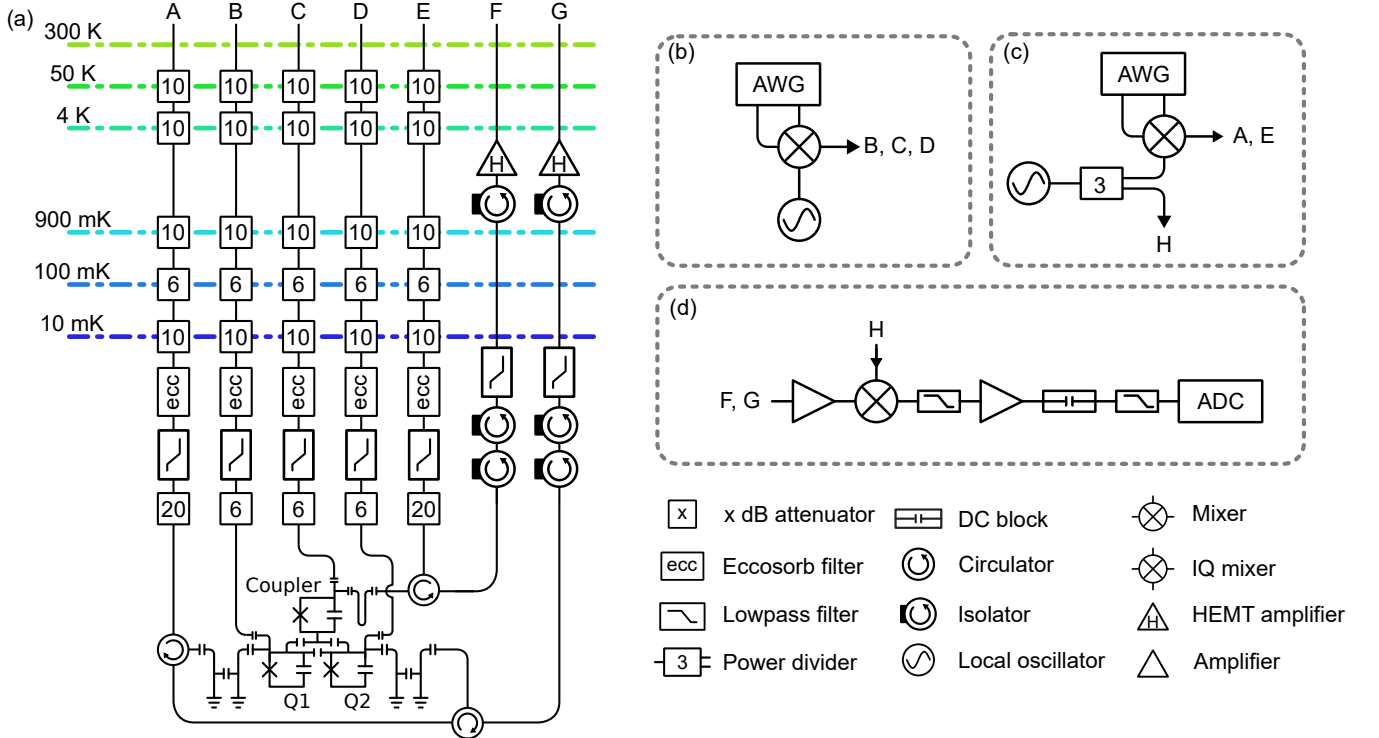


FIG. S1. Experimental setup. (a) Connections from the sample chip to ports A-G at room temperature. (b) Pulse-generating systems for qubit control. (c) Pulse-generation systems for qubit readout. (d) Readout system.

Derivation of equations

As described in the main text, the system and drive Hamiltonians we consider are

$$\hat{H} = \hat{H}_0 + \hat{H}_c \quad (\text{S1})$$

$$\hat{H}_0/\hbar = \sum_i \left(\omega_i \hat{a}_i^\dagger \hat{a}_i + \frac{\alpha_i}{2} \hat{a}_i^\dagger \hat{a}_i^\dagger \hat{a}_i \hat{a}_i \right), \quad (\text{S2})$$

$$\hat{H}_c/\hbar = \sum_{i \neq c} g_{ic} (\hat{a}_i^\dagger \hat{a}_c + \hat{a}_i \hat{a}_c^\dagger), \quad (\text{S3})$$

$$\hat{H}_d/\hbar = \Omega_d \cos \omega_d t (\hat{a}_c^\dagger + \hat{a}_c), \quad (\text{S4})$$

where $i \in \{1, 2, c\}$. By following the procedure of Schrieffer-Wolff transformation [48], we obtain an anti-Hermitian operator $\hat{S} = \hat{S}_1 + \hat{S}_2$ from the solutions of the following equations,

$$[\hat{H}_0, \hat{S}_1] + \hat{O}_1 = 0, \quad (\text{S5})$$

$$[\hat{H}_0, \hat{S}_2] + \hat{O}_2 = 0. \quad (\text{S6})$$

Here, $\hat{O}_1 = \hat{H}_c$ is considered as an off-diagonal perturbation term. We also define the diagonal and off-diagonal terms of $\frac{1}{2} [\hat{O}_1, \hat{S}_1]$ as \hat{D}_2 and \hat{O}_2 , respectively. To derive the explicit forms of \hat{S}_1 and \hat{S}_2 , we assume that each transmon is a four-level system and algebraically solve Eqs. (S5) and (S6) with a Python program. Under this setup, we first derive the CAS transition frequencies in the weak drive amplitude limit. Upon the transformation, the anti-Hermitian operators \hat{S}_1 and \hat{S}_2 cancel the off-diagonal terms in \hat{H} , and we obtain a diagonalized Hamiltonian valid up to the second order of g_{ic} ,

$$\hat{H}' = \hat{H}_0 + \hat{D}_2. \quad (\text{S7})$$

With this equation, we derive the analytical expressions of the CAS transition frequencies in the weak drive amplitude limit,

$$\begin{aligned} \omega'_b &= \langle 101 | \hat{H}' | 101 \rangle / \hbar - \langle 010 | \hat{H}' | 010 \rangle / \hbar, \\ &= \omega_c + \Delta_{12} + \frac{2g_{1c}^2(\alpha_1 + \alpha_c)}{(\Delta_{1c} - \alpha_c)(\Delta_{1c} + \alpha_1)} - \frac{2g_{2c}^2}{\Delta_{2c}}, \end{aligned} \quad (\text{S8})$$

$$\begin{aligned} \omega'_r &= \langle 011 | \hat{H}' | 011 \rangle / \hbar - \langle 100 | \hat{H}' | 100 \rangle / \hbar, \\ &= \omega_c - \Delta_{12} + \frac{2g_{2c}^2(\alpha_2 + \alpha_c)}{(\Delta_{2c} - \alpha_c)(\Delta_{2c} + \alpha_2)} - \frac{2g_{1c}^2}{\Delta_{1c}}. \end{aligned} \quad (\text{S9})$$

Next, we derive the effective CAS oscillation frequencies. We move to the reference frame rotating at ω_d and transform the drive Hamiltonian Eq. (S4) into

$$\hat{H}_d^r/\hbar \approx \frac{1}{2} \Omega (\hat{a}_c^\dagger + \hat{a}_c), \quad (\text{S10})$$

where we use the rotating-wave approximation. Note that, the form of \hat{S} is the same in the rotating frame. Using the obtained \hat{S} and the Baker-Campbell-Hausdorff formula, we expand the drive Hamiltonian Eq. (S10) as

$$\begin{aligned} e^{\hat{S}} \hat{H}_d^r e^{-\hat{S}} &= \hat{H}_d^r + [\hat{S}, \hat{H}_d^r] + \frac{1}{2!} [\hat{S}, [\hat{S}, \hat{H}_d^r]] + \dots, \\ &\approx \hat{H}_d^r + [\hat{S}_1 + \hat{S}_2, \hat{H}_d^r] + \frac{1}{2!} [\hat{S}_1, [\hat{S}_1, \hat{H}_d^r]] \equiv \hat{H}_d'^r. \end{aligned} \quad (\text{S11})$$

In the last line of the formula, we keep only the terms up to the second order of g_{ic} by assuming $|g_{ic}/\Delta_{ic}| \ll 1$. Finally, we reach the expressions of the effective CAS oscillation frequencies presented in the main text:

$$\begin{aligned}\Omega_b &\approx 2 \langle 010 | \hat{H}'_d | 101 \rangle / \hbar \\ &= \frac{2g_{1c}g_{2c}\alpha_c\Omega_d}{\Delta_{12}(\delta_c - \delta_1 + \alpha_c)(\delta_c - \delta_2)}, \\ &= \frac{2g_{1c}g_{2c}\alpha_c\Omega_d}{\Delta_{12}(\omega_c - \omega_1 + \alpha_c)(\omega_c - \omega_2)},\end{aligned}\tag{S12}$$

$$\begin{aligned}\Omega_r &\approx 2 \langle 100 | \hat{H}'_d | 011 \rangle / \hbar \\ &= \frac{-2g_{1c}g_{2c}\alpha_c\Omega_d}{\Delta_{12}(\delta_c - \delta_2 + \alpha_c)(\delta_c - \delta_1)}, \\ &= \frac{-2g_{1c}g_{2c}\alpha_c\Omega_d}{\Delta_{12}(\omega_c - \omega_2 + \alpha_c)(\omega_c - \omega_1)},\end{aligned}\tag{S13}$$

where $\delta_i = \omega_i - \omega_d$, ($i \in \{1, 2, c\}$). Moreover, we derive an analytical expression of the ac-field-dependent ZZ coupling induced by the ac Stark shift. For concreteness, we consider the case where the drive frequency ω_d is off-resonant but close to ω_b . As a first step, we expand the drive Hamiltonian using \hat{S} and then move to the reference frame rotating at ω_b , which is determined by the drive power Ω_d . Applying the rotating-wave approximation and dropping fast oscillating terms, we get the following time-dependent effective drive Hamiltonian

$$\hat{H}'_d(t)/\hbar \approx \frac{\Omega_b}{2} (|101\rangle\langle 010| e^{-i\delta t} + |010\rangle\langle 101| e^{i\delta t}),\tag{S14}$$

where $\delta = \omega_d - \omega_b$. For further analysis, we assume a form of system Hamiltonian

$$\hat{H}_{\text{sys}} = \hat{H}^{(0)} + \hat{H}(t),\tag{S15}$$

where $\hat{H}^{(0)}$ is the time-independent part and $\hat{H}(t)$ is the time-periodic part. When $\hat{H}(t)$ has the characteristic frequency ω , it can be expanded in a Fourier series of the form

$$\hat{H}(t) = \sum_{n \neq 0} \hat{H}_n e^{in\omega t}.\tag{S16}$$

We now apply the van Vleck transformation [49] and obtain the time-averaged Hamiltonian to first order

$$\hat{H}'_{\text{sys}} \approx \hat{H}^{(0)} - \frac{1}{2} \sum_{n \neq 0} \frac{[\hat{H}_{-n}, \hat{H}_n]}{n\hbar\omega}.\tag{S17}$$

Comparing Eqs. (S14) and the last terms of (S17), we obtain an expression of the ac-field-tunable part of the ZZ coupling,

$$\xi_{\text{ac}} = -\frac{\Omega_b^2}{8\delta},\tag{S18}$$

where we assume that the coupler is in the ground state. With this term, the entire ZZ interaction under the off-resonant microwave drive can be expressed as

$$\xi_{\text{ZZ}}(\omega_d, \Omega_d) = \xi_0 - \frac{\Omega_b^2}{8(\omega_d - \omega_b)},\tag{S19}$$

where $\xi_0 = \frac{2g_{\text{eff}}^2(\alpha_1 + \alpha_2)}{(\Delta_{12} + \alpha_1)(\alpha_2 - \Delta_{12})}$ is the static residual ZZ coupling that is valid up to the second order of the effective transverse coupling, $g_{\text{eff}} = \frac{g_{1c}g_{2c}}{2} \left(\frac{1}{\Delta_{1c}} + \frac{1}{\Delta_{2c}} \right) + g_{12}$, between the data qubits.

Numerical simulation method

As mentioned in the main text, we consider up to the third excited state of each transmon for numerical calculations. To evaluate the CAS oscillation frequency, we numerically diagonalize the Hamiltonian represented in the reference frame rotating at ω_d ,

$$\hat{H}_r = \hat{H}_0^r + \hat{H}_c^r + \hat{H}_d^r, \quad (\text{S20})$$

$$\hat{H}_0^r/\hbar = \sum_i \left(\delta_i \hat{a}_i^\dagger \hat{a}_i + \frac{\alpha_i}{2} \hat{a}_i^\dagger \hat{a}_i^\dagger \hat{a}_i \hat{a}_i \right), \quad (\text{S21})$$

$$\hat{H}_c^r/\hbar = \sum_{i \neq c} g_{ic} (\hat{a}_i^\dagger \hat{a}_c + \hat{a}_i \hat{a}_c^\dagger) + g_{12} (\hat{a}_1^\dagger \hat{a}_2 + \hat{a}_1 \hat{a}_2^\dagger), \quad (\text{S22})$$

$$\hat{H}_d^r/\hbar \approx \frac{1}{2} \Omega_d (\hat{a}_c^\dagger + \hat{a}_c). \quad (\text{S23})$$

Here we take into account the direct coupling g_{12} between the data transmons. For each drive amplitude Ω_d , we sweep the drive frequency ω_d and obtain the resonant CAS oscillation frequencies Ω_b (Ω_r) as the splitting at the anticrossing between the states $|010\rangle$ and $|101\rangle$ ($|100\rangle$ and $|011\rangle$).

Next, we estimate the coherence limit of the average fidelity of the CAS-based CZ gate. We use Eq. (S20) as the starting point and numerically simulate the JAZZ sequence in Fig. 3(a) in the main text. For the measurement angle 0 in the JAZZ sequence, the population of the state $|110\rangle$ ideally becomes unity at the end of the controlled phase is π . We thus numerically maximize the $|110\rangle$ population by iteratively solving the time-dependent Schrödinger equation taking account of the flat-top Gaussian pulse shape and obtaining an optimal parameter set of the drive frequency and amplitude. Note that we assume perfect accuracy of the state preparation, measurement, π -pulse, and $\pi/2$ -pulse. Using the result, we solve the master equation taking into account the coherence times shown in Table S1 and reconstruct a noisy quantum channel \mathcal{E}'_{CZ} , which is locally equivalent to a CZ gate, for the entire system. We thus apply local phase rotations to the data qubits with perfect accuracy and obtain the noisy CAS-based CZ gate channel \mathcal{E}_{CZ} . Finally, we express the average gate fidelity of a quantum channel \mathcal{E} using the following equation [50]

$$\bar{F}(\mathcal{E}) = \frac{\text{Tr}[(P_1 \otimes P_1)\mathcal{S}_{\mathcal{E}}] + \text{Tr}[P_1\mathcal{E}(P_1)]}{d(d+1)}, \quad (\text{S24})$$

where P_1 is a projector onto the d -dimensional computational subspace and $\mathcal{S}_{\mathcal{E}}$ is the superoperator form of the quantum channel \mathcal{E} . Using Eq. (S24), we evaluate the average gate fidelity of \mathcal{E}_{CZ} considering a composition between two channels $\tilde{\mathcal{E}} = \mathcal{U}_{\text{CZ}} \circ \mathcal{E}_{\text{CZ}}$, where \mathcal{U}_{CZ} is the ideal CAS-based CZ gate channel. The value obtained is $\bar{F}(\tilde{\mathcal{E}}) \approx 0.978$.

TABLE S1. Coherence times of the qubits.

	T_1 (μs)	T_2^* (μs)	T_2^c (μs)
Data transmon, Q ₁	95 ± 10	76 ± 10	88 ± 3
Data transmon, Q ₂	108 ± 6	81 ± 8	166 ± 9
Coupler transmon, Q _c	15 ± 1	15 ± 2	18 ± 2

Experiment for the ac-field tunable ZZ interaction and estimation of the direct coupling

We estimate the direct transverse coupling strength and the residual ZZ interaction strength using the JAZZ experiment described in the main text. Figure S2(a) shows a pulse sequence, where we constantly apply a relatively weak coupler drive $\Omega_d/2\pi \approx 7.3$ MHz, while sweeping the delay time τ between the echo pulses and the coupler drive detuning from the blue CAS transition, $\delta = \omega_d - \omega_b$. Furthermore, to know the sign as well as the magnitude of the ZZ interaction, the measurement angle ϕ is swept together with τ according to the relation $\phi/\tau = 2\pi \times 100$ kHz as shown in Fig. S2(b) as an example. Figure S2(c) shows the measured ZZ interaction strength ξ_{ZZ} depending on the coupler drive detuning. By fitting this modulation with numerically calculated values of the residual ZZ interaction diagonalizing Eq. (S20), we obtain the direct transverse coupling strength of $g_{12}/2\pi \simeq 1.9$ MHz. The bare residual ZZ interaction strength is also estimated to be $\xi_0/2\pi \simeq -1.5$ kHz, where all other parameters we use are presented in the main text and g_{12} is the only free parameter.

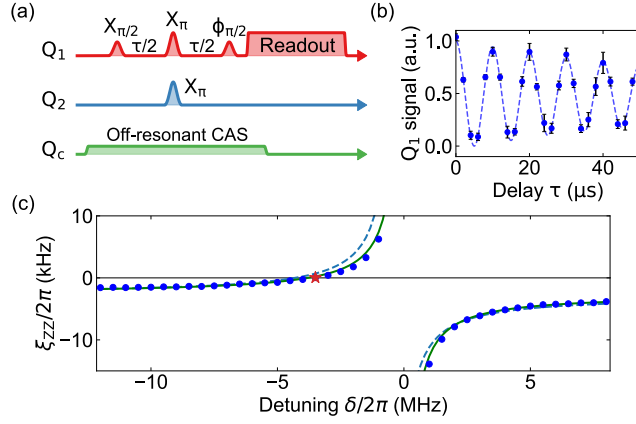


FIG. S2. (a) Pulse sequence for measuring the tunable ZZ interaction strength using the JAZZ protocol. (b) Example of the experimental data obtained with the JAZZ protocol. The data was taken at the red star shown in (c). The dashed line is the fitting curve to an exponentially decaying sinusoidal function. (c) Dependence of the ZZ interaction strength on the drive detuning from the blue CAS transition with a fixed drive power $\Omega_d/2\pi = 7.3$ MHz. The static ZZ interaction is canceled at the condition indicated by the red star. The green solid line shows the fitting result using Eq. (S19), and the blue dashed line is the numerical fit using the direct coupling g_{12} as the only free parameter.

ac Stark shift of the CAS transitions

In Figs. S3(a) and (b), we show the experimental results of the ac-Stark-shifted blue and red CAS transition frequencies as a function of the coupler drive amplitude. The CAS transition frequencies are determined by fitting the chevron pattern at each point. We model the frequency shift with the ac Stark shift of the coupler transmon $\Delta_c^{\text{ac}} = \frac{\alpha_c \Omega_d^2}{2\delta_c(\delta_c + \alpha_c)}$ [51, 52]. Using Eqs. (S8) and (S9), we define the analytically evaluated ac-Stark-shifted CAS transition frequencies as

$$\tilde{\omega}_b = \omega'_b + \Delta_c^{\text{ac}}, \quad (\text{S25})$$

$$\tilde{\omega}_r = \omega'_r + \Delta_c^{\text{ac}}, \quad (\text{S26})$$

where we ignore the ac Stark shifts of the data transmons, which are negligible compared to Δ_c^{ac} . In Figs. S3(a) and (b), we see semiquantitative agreement in the weak drive limit. The deviations between the numerical and experimental results at larger drive amplitudes could be explained by the higher-order nonlinear terms dropped in the Duffing-oscillator model [17, 53].

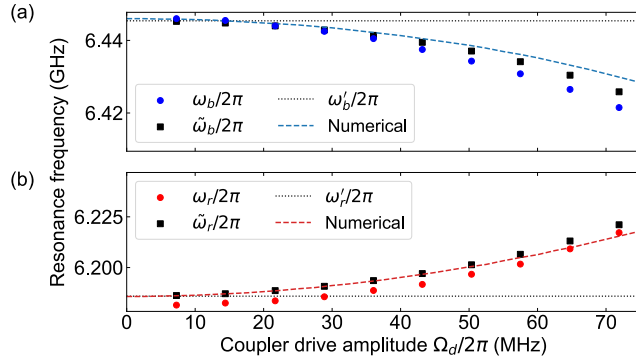


FIG. S3. Resonance frequencies of the (a) blue and (b) red CAS transitions. The filled circles are the experimental results obtained from the fitting of the chevron patterns for each drive amplitude. The filled squares are analytically calculated ac-Stark-shifted CAS transition frequencies [Eqs. (S25) and (S26)] using the same parameters as in the experiment. The dotted lines are the analytically evaluated CAS transition frequencies in the limit of the weak drive [Eqs. (S8) and (S9)]. The dashed lines are obtained numerically by diagonalizing Eqs. (S20)–(S23).

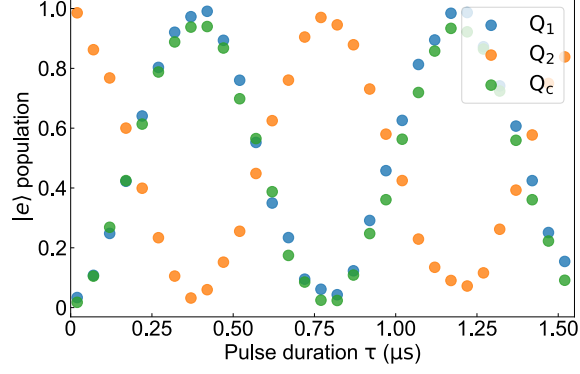


FIG. S4. Associated oscillations of the excited-state population of each transmon involved in the blue CAS transition. The vertical axis is normalized using the response signals of the ground and first-excited states of each transmon, corresponding to the excited state population of each qubit. The horizontal axis is the length of the drive pulse to the coupler transmon. The drive amplitude is $\Omega_d/2\pi \simeq 75$ MHz. Note that this data was obtained at a different cooldown from the one for the experiments in the main text.

Rabi oscillations in the blue CAS subspace

We measure the associated oscillations of the population of each qubit involved in the blue CAS transition. The pulse sequence used is identical to the one in Fig. 2(a) in the main text except for the qubits to be read out. As predicted by the theoretical model, we observe signals corresponding to the Rabi oscillations between the states $|010\rangle$ and $|101\rangle$.

Comparison of the drive efficiency and residual ZZ interaction strength with the CR gate

Lastly, we compare the expected properties of the blue CAS-based CZ gate with those of the CR gate, which is most commonly used in architectures with fixed-frequency transmons. The results are shown in Fig. S5. In both cases, we see the decrease of the residual ZZ interaction by introducing g_{12} in the regions with large enough g_{ic}/Δ_{ic} for a high drive efficiency. However, the CR gate only achieves sufficient drive efficiency η_{CR} in the regime where ξ_{ZZ} rapidly increases with g_{eff} . In contrast, the blue CAS drive efficiency is independent of g_{12} [See Eqs. (S12) and (S13)], allowing for the wide range of detuning and coupling strength with large η_b and small ξ_{ZZ} .

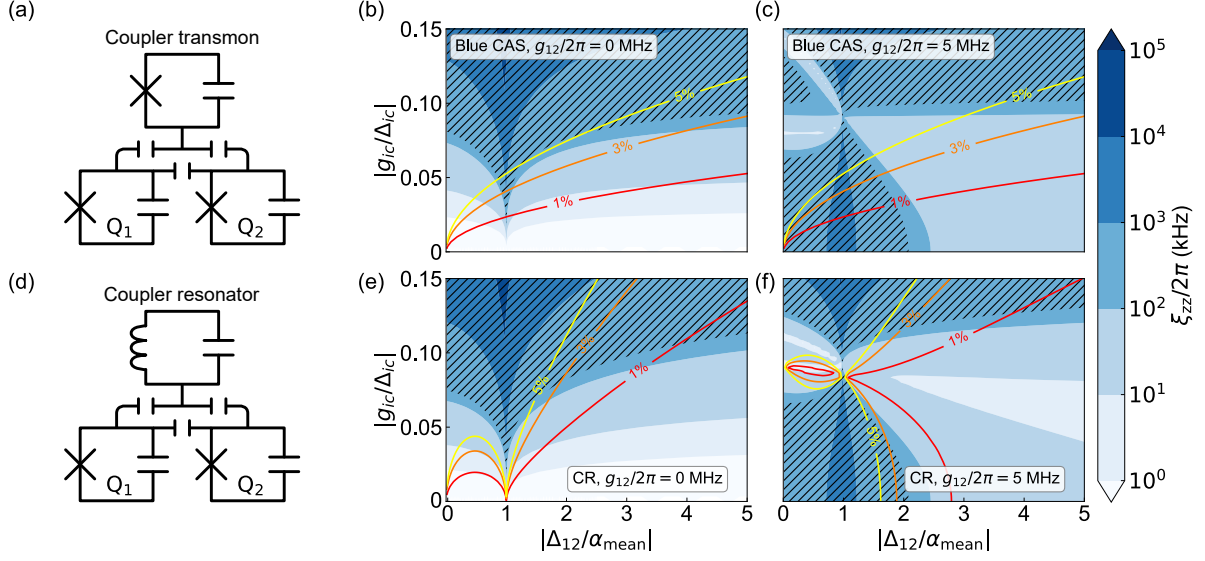


FIG. S5. (a) Circuit diagram to implement the CAS-based gates described in the main text. The residual ZZ interaction strength ξ_{ZZ} (filled contour plot) and the drive efficiency η_b of the blue CAS transition (contour line plot) are shown in (b) without and (c) with [same as in Fig. 4(b)] the direct transverse coupling g_{12} . (d) Typical circuit diagram to implement the CR gate, where we consider a linear coupler (off-resonant LC resonator) as opposed to the transmon coupler in (a). The residual ZZ interaction strength ξ_{ZZ} and drive efficiency η_{CR} of the CR gate, as a function of $|\Delta_{12}/\alpha_{\text{mean}}|$ and $|g_{ic}/\Delta_{ic}|$ are shown in (e) without and (f) with the direct transverse coupling g_{12} . Here, ξ_{ZZ} is calculated through numerical diagonalization of Eq. (S20). The drive efficiency is defined as $\eta_{CR} = 2 \times \frac{2g_{\text{eff}}\alpha_1}{\Delta_{12}(\Delta_{12} + \alpha_1)}$ from Eq. (4.26) in Ref. [54]. The additional multiplying factor of 2 explicitly indicates the fact that a $\pi/2$ -rotation of the CR gate is locally equivalent to the CNOT gate. For the calculations, we use the same parameters as in the case with the CAS transitions except for the anharmonicities of the linear coupler, $\alpha_c/2\pi = 0$ GHz, and the data transmons, $\alpha_1/2\pi = \alpha_2/2\pi = -0.3$ GHz. The latter value is typical and indeed more favorable for CR gates.